

The effect of an ordered azimuthal magnetic field on a migrating planet in a non-turbulent disc

M.L. Comins^{1*}, M.M. Romanova¹, A.V. Koldoba^{3,4}, G.V. Ustyugova³, R.V.E. Lovelace^{1,2}

¹ Department of Astronomy, Cornell University, Ithaca, NY 14853-6801, USA

² School of Applied & Engineering Physics, Cornell University, Ithaca, NY 14853-6801, USA

³ Keldysh Institute for Applied Mathematics, Moscow, Russia

⁴ Moscow Institute of Physics and Technology, Dolgoprudny, Moscow Region, 141700, Russia

25 April 2022

ABSTRACT

In this work, we consider the physics of the interaction between a planet and a magnetized gaseous protoplanetary disc. We investigate the migration of a planet in a disc that is threaded with an azimuthal magnetic field. We find that, for a larger magnetic field amplitude, there is an increasingly large positive torque on the planet from the disc, resulting in slowed and even outward migration. Our results indicate that magnetic resonances due to a purely azimuthal, ordered magnetic field can slow or stop the inward migration of Jupiter-mass, Saturn-mass, and $5M_{\oplus}$ planets.

Key words: accretion, accretion discs — magnetic fields — MHD — waves — planets and satellites: dynamical evolution and stability — planet-disc interactions

1 INTRODUCTION

There are three primary types of planet migration within a gaseous disc (Ward 1997). Type I migration occurs when a planet remains embedded in and exchanges angular momentum with the disc, and waves propagate through the disc as a result. Type II migration occurs when a planet is massive enough to open a gap in the disc, because the planet’s Hill radius exceeds the scale height of the disc. The Hill radius is defined as

$$R_{\text{H}} = r_{\text{p}} \left(\frac{M_{\text{p}}}{3M_{\star}} \right)^{1/3}, \quad (1)$$

where M_{\star} is the mass of the central star, M_{p} is the mass of the planet, and r_{p} is the orbital radius of the planet. In type III migration, material passes through the corotation region, exchanging angular momentum with the planet and causing runaway migration of the planet in the process. If the planet initially moves inward, the runaway migration direction is inward (and vice versa).

1.1 Hydrodynamic torques

The planet revolves about the star in a circular orbit with period $P = 2\pi/\Omega_{\text{p}}$, where Ω_{p} is the angular orbital frequency of the planet. Spiral density waves are excited at the disc’s Lindblad resonances when the planet tidally interacts with the disc. The angular momentum is redistributed in the disc after

the planet “dumps” angular momentum at the resonances; the disc then exerts a gravitational torque back onto the planet, consequently changing the planet’s orbital elements.

The planet excites m -armed waves in the disc with “orbital” frequencies

$$\omega = m\Omega_{\text{p}}. \quad (2)$$

The dispersion relation for the waves in a low-temperature, low-mass disc is

$$(\omega - m\Omega)^2 = \kappa^2, \quad (3)$$

where $\Omega = \Omega(r)$ is the angular frequency of the disc rotation at radius r , $\omega - m\Omega$ is the Doppler shifted frequency of the m -armed wave as seen by an observer orbiting at the disc’s angular velocity, and κ is the epicyclic frequency, which in a Keplerian disc is $\kappa = \Omega_{\text{Kep}}$. In other words,

$$m^2(\Omega - \Omega_{\text{p}})^2 = \kappa^2. \quad (4)$$

Substituting $\Omega(r) = \sqrt{GM_{\star}/r^3}$ and $\Omega_{\text{p}} = \sqrt{GM_{\star}/r_{\text{p}}^3}$, the locations of the Lindblad resonances are

$$r_{\text{LR}} = r_{\text{p}} \left(\frac{m \pm 1}{m} \right)^{2/3}. \quad (5)$$

For each value of m (except $m = 1$), there is one resonance located closer to the star than the planet ($r_{\text{ILR}} < r_{\text{p}}$), known as the “inner Lindblad resonance” (ILR), and one located farther from the star than the planet ($r_{\text{OLR}} > r_{\text{p}}$), known as the “outer Lindblad resonance” (OLR). The parts of the disc interior to the planet exert a positive torque on the planet and “push” the planet outward, while the parts of

* e-mail: mcomins@astro.cornell.edu

the disc exterior to the planet exert a negative torque on the planet and push the planet inward.

The torques exerted on the planet from each ILR and OLR are different in magnitude and opposite in sign; the sum of these torques is referred to as the “differential Lindblad torque.” The sign of the differential Lindblad torque indicates the direction in which the planet will migrate. The differential Lindblad torque on the disc from the planet, as calculated by Tanaka et al. (2002), is

$$\Gamma_{\text{total}} \propto \left(\frac{M_{\text{p}} r_{\text{p}} \Omega_{\text{p}}}{c_s M_{\star}} \right)^2 \Sigma(r_{\text{p}}) r_{\text{p}}^4 \Omega_{\text{p}}^2 > 0, \quad (6)$$

where $\Sigma(r_{\text{p}})$ and c_s are the surface density and isothermal sound speed in the disc at the orbital radius of the planet, respectively. This implies that the torque on the planet from the disc is negative, $\Gamma_{\text{total}} < 0$, resulting in inward migration of the planet as it loses angular momentum to the disc.

There is also a torque from the material corotating with the planet, of which two primary contributors are the entropy- and vortensity-related torques, where vortensity is defined as the ratio of the local vorticity to the surface density in the disc:

$$\eta = \frac{\nabla \times \mathbf{v}}{\Sigma}. \quad (7)$$

The corotation torque connected with vortensity is proportional to gradient of the vortensity across the corotation region about the planet (Masset 2001). The corotation torque connected with the entropy is, analogously, proportional to the gradient of the entropy across this same region (Paardekooper et al. 2010). Both of these corotation torques can exert a positive torque on the planet, and the (positive) magnitude of the total corotation torques can exceed the magnitude of the (negative) differential Lindblad torque, possibly resulting in overall outward planet migration. The specific details of these corotation torques are outside the scope of this paper, but see, e.g., Paardekooper & Mellema (2006); Baruteau & Masset (2008); Paardekooper & Papaloizou (2008); Kley et al. (2009); Masset & Casoli (2009, 2010); Paardekooper et al. (2010, 2011) for more details.

1.2 MHD torque

When there exists a magnetic field in the disc, magnetic resonances can appear that can also exert a significant torque on the planet (e.g., Terquem 2003; Fromang et al. 2005; Fu & Lai 2011). Terquem (2003) calculated the linear torque on a planet in a fixed circular orbit and found that magnetic resonances can be generated near the planet, and that tightly wound waves can be generated near these resonances. The frequency of the waves excited by the planet is equal to the Doppler-shifted frequency of a slow MHD wave that is propagating along the field lines in the disc (Terquem 2003),

$$m^2(\Omega - \Omega_{\text{p}})^2 = \frac{m^2 c_s^2 v_{\text{A}}^2}{r^2(v_{\text{A}}^2 + c_s^2)}. \quad (8)$$

Here, m cancels out and v_{A} is the Alfvén speed, given by Terquem (2003) as

$$v_{\text{A}}^2 = \frac{\langle B^2 \rangle}{\mu_0 \Sigma}, \quad (9)$$

where $\langle B^2 \rangle$ is the vertically-integrated square of the magnetic field. The locations of the inner magnetic resonance (IMR)

and outer magnetic resonance (OMR), according to Terquem (2003), are, respectively,

$$r_{\text{IMR}} = r_{\text{p}} - \frac{2c_s}{3\Omega} \frac{1}{\sqrt{1 + v_{\text{A}}^2/c_s^2}} \quad (10)$$

and

$$r_{\text{OMR}} = r_{\text{p}} + \frac{2c_s}{3\Omega} \frac{1}{\sqrt{1 + v_{\text{A}}^2/c_s^2}}, \quad (11)$$

respectively. Here, v_{A} , c_s , and Ω are again evaluated at the location of the planet. The waves associated with these resonances can propagate interior and exterior to the Lindblad resonances, as well as between the resonances.

The ratio between the matter and magnetic pressure in the disc is $\beta \equiv c_s^2/v_{\text{A}}^2$. If the magnitude of β near the planet (i.e., between the magnetic resonances) is low enough in magnitude, the waves associated with the magnetic resonances can exert a positive torque that is larger in magnitude than the differential Lindblad torque.

Magnetic resonances can be important to planet migration in any part of the disc in which a magnetic field is present. This includes the region of the disc in which planets are thought to form (i.e., 1 – 5 AU), as well as distances less than 0.1 AU, which is near the stellar magnetosphere, where the field lines of the external magnetosphere can produce a significant azimuthal component of the field due to the differential rotation in the disc.

Fromang et al. (2005) performed simulations of both a planet in a fixed circular orbit and one that is allowed to migrate and found, using 2D MHD simulations in a non-turbulent disc that the inward migration of a low-mass planet ($5M_{\oplus}$) can be reversed by the torque from the magnetic resonances. A more recent paper by Guilet et al. (2013) studied the effects of an MHD corotation torque on a similarly low-mass planet in a 2D laminar disc with a weak azimuthal field threading the disc. The field was not strong enough to generate an appreciable torque from magnetic resonances, and it was not strong enough to dominate the hydrodynamic corotation torques, but a “torque excess” attributed to the presence of the magnetic field was found. Their results correspond to the work done by Baruteau et al. (2011) and Uribe et al. (2011), which showed the existence of additional MHD corotation torques in MRI-turbulent discs using 3D MHD simulations.

The aim of this paper is to study how the torque exerted on the planet by magnetic resonances affects the migration of a planet in a non-turbulent two-dimensional disc threaded by an initially azimuthal magnetic field. We study how the total gravitational torque and semimajor axis evolves in cases of different planet masses and the magnetic field amplitudes, while the disc mass is kept constant.

The plan of this paper is as follows. In §2 we describe our physical model and numerical setup. In §3 we discuss the impact of a magnetic field on the surface density of the disc nearby the planet for several different planet masses. In §4, we discuss the effects of a magnetic field on the total torque on the planet over time. In §5 we describe the impact of a magnetic field on the semimajor axis change for several planet masses. In §6, we discuss converting our data into dimen-

sional units, including the migration times of our simulated planets. Finally, in §7, we discuss our conclusions.

2 MODEL

2.1 MHD Equations

We utilize the MHD equations to numerically evaluate the perturbative effect of the planet on the disc:

(i) Continuity equation (conservation of mass)

$$\frac{\partial \Sigma}{\partial t} + \frac{1}{r} \frac{\partial}{\partial r} (r \Sigma v_r) + \frac{1}{r} \frac{\partial}{\partial \varphi} (\Sigma v_\varphi) = 0, \quad (12)$$

where $\Sigma = \int \rho dz$ is the surface density (with ρ the volume density), and v_r and v_φ are the radial and azimuthal velocities, respectively.

(ii) Radial equation of motion (conservation of momentum)

$$\begin{aligned} \frac{\partial}{\partial t} (\Sigma v_r) + \frac{1}{r} \frac{\partial}{\partial r} \left[r \left(\Sigma v_r^2 + \Pi + \frac{\Psi_{rr} + \Psi_{\varphi\varphi}}{8\pi} - \frac{\Psi_{r\varphi}}{4\pi} \right) \right] \\ + \frac{1}{r} \frac{\partial}{\partial \varphi} \left(\Sigma v_r v_\varphi - \frac{\Psi_{r\varphi}}{4\pi} \right) \\ = \frac{\Pi}{r} + \frac{\Psi_{rr} + \Psi_{\varphi\varphi}}{8\pi r} - \Sigma \frac{GM_\star}{r^2} + \Sigma w_r, \end{aligned} \quad (13)$$

where $\Pi = \int p dz$ is the surface pressure (with p the volume pressure), and Σw_r is the radial force exerted on the disc by the planet (per unit area of the disc), and Ψ_{rr} , $\Psi_{r\varphi}$, and $\Psi_{\varphi\varphi}$ are magnetic surface variables which are discussed in more detail in §2.1.1.

(iii) Azimuthal equation of motion (conservation of angular momentum)

$$\begin{aligned} \frac{\partial}{\partial t} (\Sigma v_\varphi) + \frac{1}{r^2} \frac{\partial}{\partial r} \left[r^2 \left(\Sigma v_r v_\varphi - \frac{\Psi_{r\varphi}}{4\pi} \right) \right] \\ + \frac{1}{r} \frac{\partial}{\partial \varphi} \left(\Sigma v_\varphi^2 + \Pi + \frac{\Psi_{rr} + \Psi_{\varphi\varphi}}{8\pi} - \frac{\Psi_{\varphi\varphi}}{4\pi} \right) \\ = \Sigma w_\varphi, \end{aligned} \quad (14)$$

where Σw_φ is the azimuthal force exerted on the disc by the planet (per unit area of the disc).

(iv) Radial induction equation

$$\frac{\partial \Phi_r}{\partial t} + \frac{1}{r} \frac{\partial}{\partial \varphi} (v_\varphi \Phi_r - v_r \Phi_\varphi) = 0, \quad (15)$$

where Φ_r and Φ_φ are different magnetic surface variables, also discussed in §2.1.1.

(v) Azimuthal induction equation

$$\frac{\partial \Phi_\varphi}{\partial t} + \frac{\partial}{\partial r} (v_r \Phi_\varphi - v_\varphi \Phi_r) = 0. \quad (16)$$

(vi) Entropy balance equation

$$\frac{\partial}{\partial t} [\Sigma K] + \frac{1}{r} \frac{\partial}{\partial r} [r \Sigma K v_r] + \frac{1}{r} \frac{\partial}{\partial \varphi} (\Sigma K v_\varphi) = 0, \quad (17)$$

where $K = \Pi/\Sigma^\gamma$ is a function analogous to entropy, and $\gamma = 5/3$ is the adiabatic index for a monatomic ideal gas.

Moreover, following the α prescription of Shakura & Sunyaev (1973), we use a very small viscosity ($\alpha = 0.001$) to isolate the effects of slow magnetosonic waves in the disc by smoothing out the effects of fast magnetosonic waves in the disc.

2.1.1 Magnetic surface variables

The “volume” values for the radial and azimuthal magnetic fields are given by B_r and B_φ .

The usage of surface values for the variables related to the magnetic field are not as easily defined and used as Σ and Π , and so we describe them in detail here. The “volume” values for the radial and azimuthal magnetic fields are given by B_r and B_φ . The vertically-integrated fields may be defined as $\Phi_r = \int B_r dz$ and $\Phi_\varphi = \int B_\varphi dz$, as done with Σ and Π . There are also terms involving magnetic flux or energy that involve products of these variables: B_r^2 , B_φ^2 , and $B_r B_\varphi$. We define the following vertically-integrated quantities: $\Psi_{rr} = \int B_r^2 dz$, $\Psi_{r\varphi} = \int B_r B_\varphi dz$, and $\Psi_{\varphi\varphi} = \int B_\varphi^2 dz$.

As shown above, the induction equations use Φ_r and Φ_φ , while the equations of motion use Ψ_{rr} , $\Psi_{r\varphi}$, and $\Psi_{\varphi\varphi}$. As such, we need a way to relate Φ and Ψ . We can do this using a “magnetic” thickness of the disc, H . Using the definitions of Φ and Ψ , with H , we find that

$$\Psi_{rr} = \frac{\Phi_r \Phi_r}{H}; \quad \Psi_{r\varphi} = \frac{\Phi_r \Phi_\varphi}{H}; \quad \Psi_{\varphi\varphi} = \frac{\Phi_\varphi \Phi_\varphi}{H}. \quad (18)$$

We suggest that the coefficient H is the same in all three relations.

By relating Φ and Ψ in this way, we can define one more variable related to the magnetic field such that the MHD equations are parameterized with respect to a single magnetic field variable,

$$\mathfrak{B}_r = \frac{\Phi_r}{\sqrt{H}}; \quad \mathfrak{B}_\varphi = \frac{\Phi_\varphi}{\sqrt{H}}. \quad (19)$$

Then, the magnetic terms in Equations (13) - (16) take their usual form. The radial equation of motion becomes

$$\begin{aligned} \frac{\partial}{\partial t} (\Sigma v_r) + \frac{1}{r} \frac{\partial}{\partial r} \left[r \left(\Sigma v_r^2 + \Pi + \frac{\mathfrak{B}_r^2 + \mathfrak{B}_\varphi^2}{8\pi} - \frac{\mathfrak{B}_r \mathfrak{B}_\varphi}{4\pi} \right) \right] \\ + \frac{1}{r} \frac{\partial}{\partial \varphi} \left(\Sigma v_r v_\varphi - \frac{\mathfrak{B}_r \mathfrak{B}_\varphi}{4\pi} \right) \\ = \frac{\Sigma v_r^2}{r} + \frac{\Pi}{r} + \frac{\mathfrak{B}_r^2 + \mathfrak{B}_\varphi^2}{8\pi r} \\ - \Sigma \frac{GM_\star}{r^2} + \Sigma w_r, \end{aligned} \quad (20)$$

and the azimuthal equation of motion becomes

$$\begin{aligned} \frac{\partial}{\partial t} (\Sigma v_\varphi) + \frac{1}{r^2} \frac{\partial}{\partial r} \left[r^2 \left(\Sigma v_r v_\varphi - \frac{\mathfrak{B}_r \mathfrak{B}_\varphi}{4\pi} \right) \right] \\ + \frac{1}{r} \frac{\partial}{\partial \varphi} \left(\Sigma v_\varphi^2 + \Pi + \frac{\mathfrak{B}_r^2 + \mathfrak{B}_\varphi^2}{8\pi} - \frac{\mathfrak{B}_\varphi^2}{4\pi} \right) \\ = \Sigma w_\varphi. \end{aligned} \quad (21)$$

For simplicity, we accept that $H = \text{const}$. Then, the radial and azimuthal induction equations become, respectively,

$$\frac{\partial \mathfrak{B}_r}{\partial t} + \frac{1}{r} \frac{\partial}{\partial \varphi} (v_\varphi \mathfrak{B}_r - v_r \mathfrak{B}_\varphi) = 0. \quad (22)$$

and

$$\frac{\partial \mathfrak{B}_\varphi}{\partial t} + \frac{\partial}{\partial r} (v_r \mathfrak{B}_\varphi - v_\varphi \mathfrak{B}_r) = 0. \quad (23)$$

2.2 Planetary equation of motion

We calculate the equations of motion in the stellar reference frame. This system is not inertial, because the star (due to the

gravitational influence from the planet and disc) also revolves about the center of mass of the system. Thus, the inertial force is added to the equation of motion for both the disc and the planet. Assuming that the inertial acceleration is only due to the gravitational attraction between the star and the planet (but not the disc), the inertial force per unit mass (i.e., acceleration) is

$$\mathbf{w}_i = -\frac{GM_p}{r_p^3} \mathbf{r}_p. \quad (24)$$

The total acceleration is then

$$\mathbf{w} = \mathbf{w}_p + \mathbf{w}_i, \quad (25)$$

which is converted into polar coordinates to obtain w_r and w_φ .

We use the same gravitational potential as that used in the three-dimensional simulations in Kley et al. (2009) and Klahr & Kley (2006),

$$\Phi = -\frac{GM_\star}{r} + \Phi_p, \quad (26)$$

where Φ_p reflects the gravitational influence of the planet on the disc,

$$\Phi_p = \begin{cases} -\frac{GM_p}{d} \left[\left(\frac{d}{r_{\text{sm}}} \right)^4 - 2 \left(\frac{d}{r_{\text{sm}}} \right)^3 + 2 \frac{d}{r_{\text{sm}}} \right] & \text{for } d \leq r_{\text{sm}} \\ -\frac{GM_p}{d} & \text{for } d > r_{\text{sm}}, \end{cases} \quad (27)$$

with $d = |\mathbf{r} - \mathbf{r}_p|$ being the distance between the planet and a point in the disc, and r_{sm} the smoothing radius. We use a smoothing radius of $r_{\text{sm}} = 0.8R_H$, where R_H is the Hill radius. Although our simulations are two-dimensional, we use this potential in anticipation of future three-dimensional work.

We use this potential to calculate the force from the planet on each of the fluid elements in the disc (per unit mass):

$$\mathbf{w}_p = -\nabla\Phi_p = \begin{cases} -\frac{GM_p}{r_{\text{sm}}^3} \left(\frac{3d}{r_{\text{sm}}} - 4 \right) \mathbf{d} & \text{for } d \leq r_{\text{sm}} \\ -\frac{GM_p}{d^3} \mathbf{d} & \text{for } d > r_{\text{sm}}. \end{cases} \quad (28)$$

The force exerted on the planet by a particular fluid element is the acceleration with opposite sign, multiplied by the mass of the fluid element,

$$d\mathbf{f} = -dM\mathbf{w} = dM(\nabla\Phi_p - \mathbf{w}_i), \quad (29)$$

where $dM = \Sigma r dr d\varphi$. We then calculate the total force exerted on the planet by the disc by integrating over the disc within the computational domain,

$$\mathbf{F}_{\text{disc} \rightarrow \text{p}} = \int_{\text{disc}} \psi d\mathbf{f} = \int_{\text{disc}} \psi (\mathbf{w}_i - \nabla\Phi_p) dM, \quad (30)$$

where ψ is a tapering function used to exclude the inner parts of the planet's Hill sphere from the force (Kley et al. 2009):

$$\psi = \left[\exp \left(\frac{r_{\text{sm}} - d}{0.1r_{\text{sm}}} \right) + 1 \right]^{-1}. \quad (31)$$

We use the planet's equation of motion to find the position, \mathbf{r}_p , and velocity, \mathbf{v}_p , of the planet at each time step:

$$M_p \frac{d\mathbf{v}_p}{dt} = -\frac{GM_\star M_p}{r_p^3} \mathbf{r}_p - \frac{GM_p^2}{r_p^3} \mathbf{r}_p + \mathbf{F}_{\text{disc} \rightarrow \text{p}}. \quad (32)$$

In addition to this, we calculate the planet's orbital semi-major axis, a , and eccentricity, e , to describe the general properties of its orbit. These orbital elements were calculated via the planet's orbital energy and angular momentum per unit mass (Murray & Dermott 1999):

$$E = \frac{1}{2} |\mathbf{v}_p|^2 - \frac{GM_\star}{a}, \quad (33)$$

$$\mathbf{h} = \mathbf{r}_p \times \dot{\mathbf{r}}_p, \quad (34)$$

$$a = -\frac{1}{2} \frac{GM_\star}{E}, \quad (35)$$

and

$$e = \sqrt{1 - \frac{h^2}{GMa}}. \quad (36)$$

The gravitational torque in the z direction on the planet is the sum over the torques from each fluid element: $T_z = \int_{\text{disc}} [\mathbf{r} \times \psi d\mathbf{f}]_z$. Effectively, torques due to the magnetic resonances alter the disc's surface density profile, which then alters the gravitational torque on the planet.

2.3 Reference units

Our code uses dimensionless variables; for each dimensionless quantity, \tilde{Q} , the physical quantity, Q , is recovered via

$$Q = Q_0 \tilde{Q}, \quad (37)$$

where Q_0 is a "reference quantity" that converts the simulation variables into their dimensional counterparts. The value of Q_0 is chosen to reflect realistic astrophysical systems.

We choose the mass of the star, M_\star , and the reference distance, r_0 . The reference velocity is the Keplerian orbital velocity, $v_0 = \sqrt{GM_\star/r_0}$. The reference time scale is defined as $t_0 = r_0/v_0$, and the reference rotational period is $P_0 = 2\pi t_0$. The inner and outer radii of the simulation region are given by $r_{\text{in}} = r_0$ and $r_{\text{out}} \approx 33r_0$, and a disc height typical for a protoplanetary disc is chosen ($H = 0.05r_0$).

We choose the mass of the planet relative to the mass of the star, $M_p = \tilde{m}_p M_\star$. We also introduce a characteristic mass of the disc, $M_d = \tilde{m}_d M_\star$, in which $\tilde{m}_d = \kappa \tilde{m}_p$. Because the disc mass can be altered via both M_p and κ , changing the planet mass requires a compensating change in κ in order to keep the mass of the disc constant. For $M_p = M_{\text{Jup}}$, $\tilde{m}_p = 10^{-3}$ and $\kappa = 1$. Thus, because (approximately) $M_{\text{Sat}} = 0.3M_{\text{Jup}}$, $\tilde{m}_p = 3 \times 10^{-4}$ and $\kappa = 3$ for the case of a Saturn-mass planet. Also, $5M_\oplus = 0.015M_{\text{Jup}}$, and so $\tilde{m}_p = 1.5 \times 10^{-5}$ and $\kappa = 66.67$ for the case of a $5 M_\oplus$ planet. The reference surface density is $\Sigma_0 = M_d/r_0^2$.

To find the characteristic reference value for the magnetic field, B_0 , we utilize the previously-defined surface magnetic field \mathfrak{B} ,

$$\mathfrak{B}_0^2 = B_0^2 r_0. \quad (38)$$

Furthermore, we can vertically integrate $B_0^2 = \rho_0 v_0^2$ to attain

$$\mathfrak{B}_0^2 = \Sigma_0 v_0^2. \quad (39)$$

Combining Equations (38) and (39) yields B_0 :

$$B_0 = \sqrt{\Sigma_0 v_0^2 / r_0}. \quad (40)$$

The values for our reference quantities are shown in Table 1. Note that, because the migration time scale for an embedded planet is inversely proportional to the disc's surface

Variable	Meaning	Value
r_0	Reference distance scale	0.5 AU 7.48×10^{12} cm
M_\star	Stellar mass	$1M_\odot$ 1.989×10^{33} g
v_0	Reference (Keplerian) velocity	42.1 km s $^{-1}$
t_0	Reference timescale	20.6 days
P_0	Reference (Keplerian) rotation period	129 days
M_d	Reference (disc) mass	1.989×10^{30} g
Σ_0	Reference disc surface density	3.55×10^4 g cm $^{-2}$
B_0	Reference magnetic field strength	0.29 kG

Table 1. Reference units. See a more detailed description in §2.3.

density, we are able to reduce the computational time necessary to see migration by increasing the surface density; this is why we use a large surface density for Σ_0 . For more details, please see §6.

2.4 Initial conditions

In order to accurately model this system, we must establish quasi-equilibrium initial conditions, such that the disc is approximately in mechanical equilibrium. Quasi-equilibrium between the rotation, pressure, and gravity of the system is achieved following a method similar to that described in, e.g., §2.4 of Romanova et al. (2002), Ustyugova et al. (2006) and Dyda et al. (2013).

The initial pressure at $r = r_0$ is Π_0 , and the disc is initially barotropic, such that

$$\Sigma(\Pi) = \frac{\Pi}{T_d}, \quad (41)$$

where T_d is the temperature in the disc¹. This implies that the pressure can be calculated using Bernoulli's equation

$$F + \Phi_c + \Phi = W = \text{constant}. \quad (42)$$

Here $\Phi = -GM_\star/r$ is the gravitational potential, Φ_c is the centrifugal potential

$$\Phi_c(r) = k \frac{GM_\star}{r}, \quad (43)$$

where k characterizes how different the disc is from Keplerian (i.e., our disc is slightly sub-Keplerian in order to balance the pressure gradient, such that $k = 0.975$), and F is

$$F = \int_{\Pi_0}^{\Pi} \frac{d\Pi}{\Sigma} = T_d \int_{\Pi_0}^{\Pi} \frac{d\Pi}{\Pi} = T_d \ln \left(\frac{\Pi}{\Pi_0} \right). \quad (44)$$

At $r = r_0$, $F = 0$ and

$$W = \Phi(r_0) + \Phi_c(r_0) = (k - 1) \frac{GM_\star}{r_0}. \quad (45)$$

By calculating Φ and Φ_c throughout the disc, we can use $F =$

¹ Π_0 does not denote a reference value here; it is instead defined as $\Pi_0 \equiv \Pi(r_{\text{in}}) = \Pi(r_0)$.

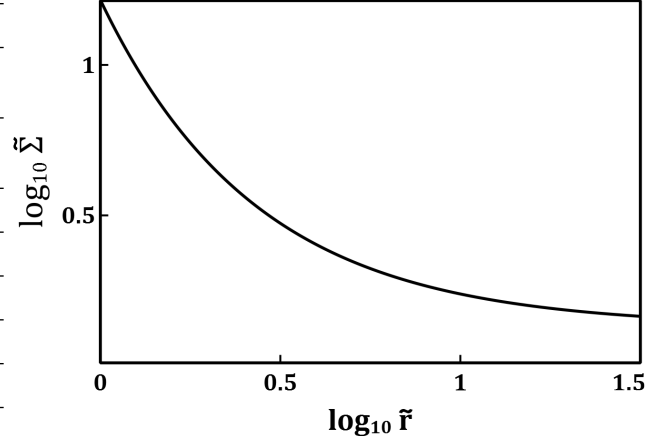


Figure 1. Initial radial surface density profile for all cases.

$W - (\Phi + \Phi_c)$ to calculate the pressure distribution in the disc,

$$\Pi = \Pi_0 \exp \left(\frac{F}{T_d} \right). \quad (46)$$

Then, the initial density distribution is (shown in Fig. 1)

$$\Sigma = \frac{\Pi}{T_d} = \frac{\Pi_0}{T_d} \exp \left(\frac{F}{T_d} \right). \quad (47)$$

The magnetic field is initialized as purely toroidal via

$$\mathfrak{B}_\varphi = \frac{b}{r} \hat{\varphi}. \quad (48)$$

Varying the magnetic field amplitude via b effectively changes the initial location of the $\beta = 1$ surface relative to the planet. In this work, we define β as

$$\beta \equiv \frac{\Pi}{\mathfrak{B}^2/8\pi}. \quad (49)$$

The initial radial distribution of $\tilde{\mathfrak{B}}_\varphi$ through the disc is shown in Fig. 2 for several values of the field amplitude, and Fig. 3 shows the initial surface density for all cases, with the $\beta = 1$ lines shown for several different magnetic field amplitudes. The positions of the $\beta = 1$ lines relative to the initial orbital radius of the planet (at $\tilde{r} = 5$) indicate that we are in an intermediate to strong range of magnetic field strengths.

2.5 Grid and boundary conditions

We use a uniform polar grid in the r and φ directions, with N_r defined to be the number of radial grid cells and N_φ the number of azimuthal grid cells. We use a fixed boundary condition at the inner boundary and outflow boundary conditions at the outer boundary for the surface density and pressure, as well as for the surface magnetic field and velocity components.

We apply a wave damping algorithm near the inner boundary similar to the method used in Section 3.2 of de Val-Borro et al. (2006) to avoid nonphysical wave reflections. We damp waves after every time step for $\tilde{r} < \tilde{r}_{\text{damp}}$, where $\tilde{r}_{\text{damp}} = 1.375$, similar to the inner damping region chosen in de Val-Borro et al. (2006). We define a coefficient:

$$\mathcal{J} = 1 + \frac{\Delta \tilde{t}}{\tilde{P}_{\text{orb}}} \left(\frac{\tilde{r}_{\text{damp}} - \tilde{r}}{\tilde{r}_{\text{damp}} - \tilde{r}_{\text{in}}} \right)^2, \quad (50)$$

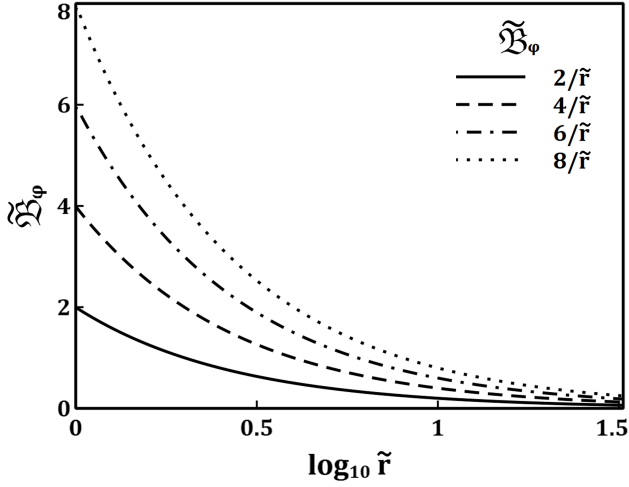


Figure 2. Initial radial profile of $\tilde{\mathfrak{B}}_\varphi$ through the disc, for $\tilde{\mathfrak{B}}_\varphi = 2/\tilde{r}$ (solid line), $\tilde{\mathfrak{B}}_\varphi = 4/\tilde{r}$ (dashed line), $\tilde{\mathfrak{B}}_\varphi = 6/\tilde{r}$ (dash-dotted line), and $\tilde{\mathfrak{B}}_\varphi = 8/\tilde{r}$ (dotted line).

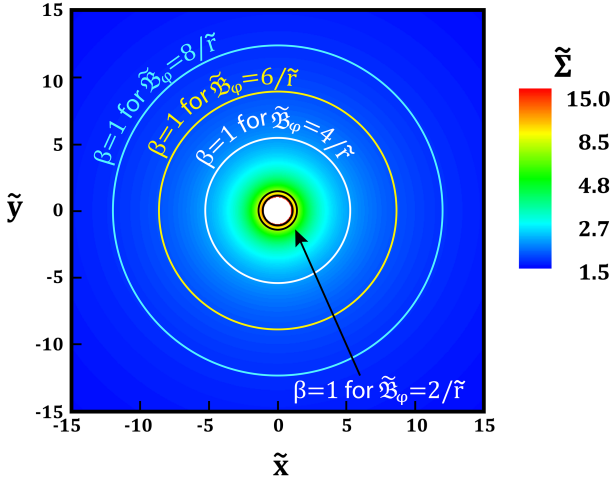


Figure 3. The initial surface density for all cases, with the location of the $\beta = 1$ surface superimposed on the disc for several magnetic field amplitudes: $\tilde{\mathfrak{B}}_\varphi = 2/\tilde{r}$ (black), $\tilde{\mathfrak{B}}_\varphi = 4/\tilde{r}$ (white), $\tilde{\mathfrak{B}}_\varphi = 6/\tilde{r}$ (yellow), and $\tilde{\mathfrak{B}}_\varphi = 8/\tilde{r}$ (cyan).

where $\Delta\tilde{t}$ is the current time step and \tilde{P}_{orb} is the Keplerian orbital period at \tilde{r} . Then, in the damping region (i.e., $\tilde{r} < \tilde{r}_{\text{damp}}$), we apply the following damping conditions,

$$\tilde{v}_{r,\text{damp}} = \tilde{v}_{r,\text{init}} + \mathcal{J}(\tilde{v}_r - \tilde{v}_{r,\text{init}}), \quad (51)$$

$$\tilde{v}_{\varphi,\text{damp}} = \tilde{v}_{\varphi,\text{init}} + \mathcal{J}(\tilde{v}_\varphi - \tilde{v}_{\varphi,\text{init}}), \quad (52)$$

and

$$\tilde{\Sigma}_{\text{damp}} = \tilde{\Sigma}_{\text{init}} + \mathcal{J}(\tilde{\Sigma} - \tilde{\Sigma}_{\text{init}}), \quad (53)$$

where $\tilde{v}_{r,\text{init}} = 0$ and $\tilde{v}_{\varphi,\text{init}} = \tilde{v}_{\text{Kep}}$ are the (dimensionless) initial radial and azimuthal velocities, respectively. Finally, the entropy is updated using the damped surface density value.

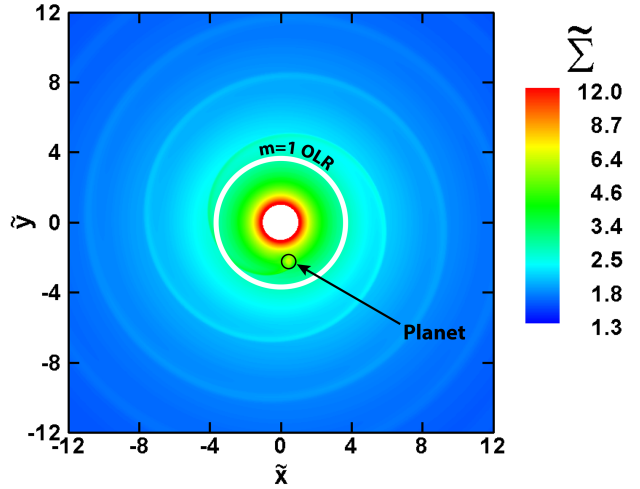


Figure 4. The surface density distribution for $\tilde{\mathfrak{B}}_\varphi = 0$ (hydrodynamic case) at $\tilde{t} = 100$ for the case of a Jupiter-mass planet. The $m = 1$ OLR location is labeled and shown by the solid white circle; the planet's location is shown by the solid black circle of arbitrary size. Of the possible Lindblad resonances, we choose to show only the $m = 1$ OLR and the one-armed spiral wave excited by this resonance.

3 CHANGE IN $\tilde{\Sigma}$ AND β NEAR THE PLANET

Fig. 4 shows the surface density distribution at $\tilde{t} = 100$ for the hydrodynamic model in the case of a Jupiter-mass planet. We only display out to $\tilde{r} = 12$ in this figure to highlight variations in $\tilde{\Sigma}$ more clearly. The planet is indicated with a solid black circle of arbitrary size, and the location of the $m = 1$ outer Lindblad resonance is labeled. The primary driver of migration in this case is the differential Lindblad torque, of which the torque from the $m = 1$ OLR is the largest contributor.

Fig. 5 shows the density distribution at $\tilde{t} = 600$ for the MHD model with $\tilde{\mathfrak{B}}_\varphi = 6/\tilde{r}$ for the case of a Jupiter-mass planet. The one-armed spiral wave associated with the $m = 1$ OLR is also seen here, but it appears relatively more “smeared out” than in the hydrodynamic case. The two indicated regions in Fig. 5, A and B, are examined in more detail in Figs. 6 and 7. Region A was chosen to show the disc properties very near the planet, while region B was chosen to show the disc properties near the planet’s orbital radius but not near the planet itself. In all of the following plots in this section, the locations of the $m = 1$ OLR, the $m = 2$ ILR and OLR, the IMR and OMR, and the planet are labeled.

Figures 6 and 7 show the $\tilde{\Sigma}$ and β distributions in regions A and B, respectively. In each of these plots, $\tilde{\Sigma}$ or β is sampled along a scanline; the scanline is indicated by a straight dotted line in the contour plot. The one-dimensional profile of the quantity sampled along the scanline ($\tilde{\Sigma}$ or β) is shown below the contour plot. The x-axis of both plots are the same and are lined up such that the two plots can be directly compared and variations in $\tilde{\Sigma}$ or β can be more easily shown.

In Fig. 6, the surface density is relatively higher at the planet’s location than in the region between the planet and the magnetic resonances. This is more clearly seen in the one-dimensional profile of $\tilde{\Sigma}$ sampled along the indicated scanline. Even with the non-constant underlying surface density

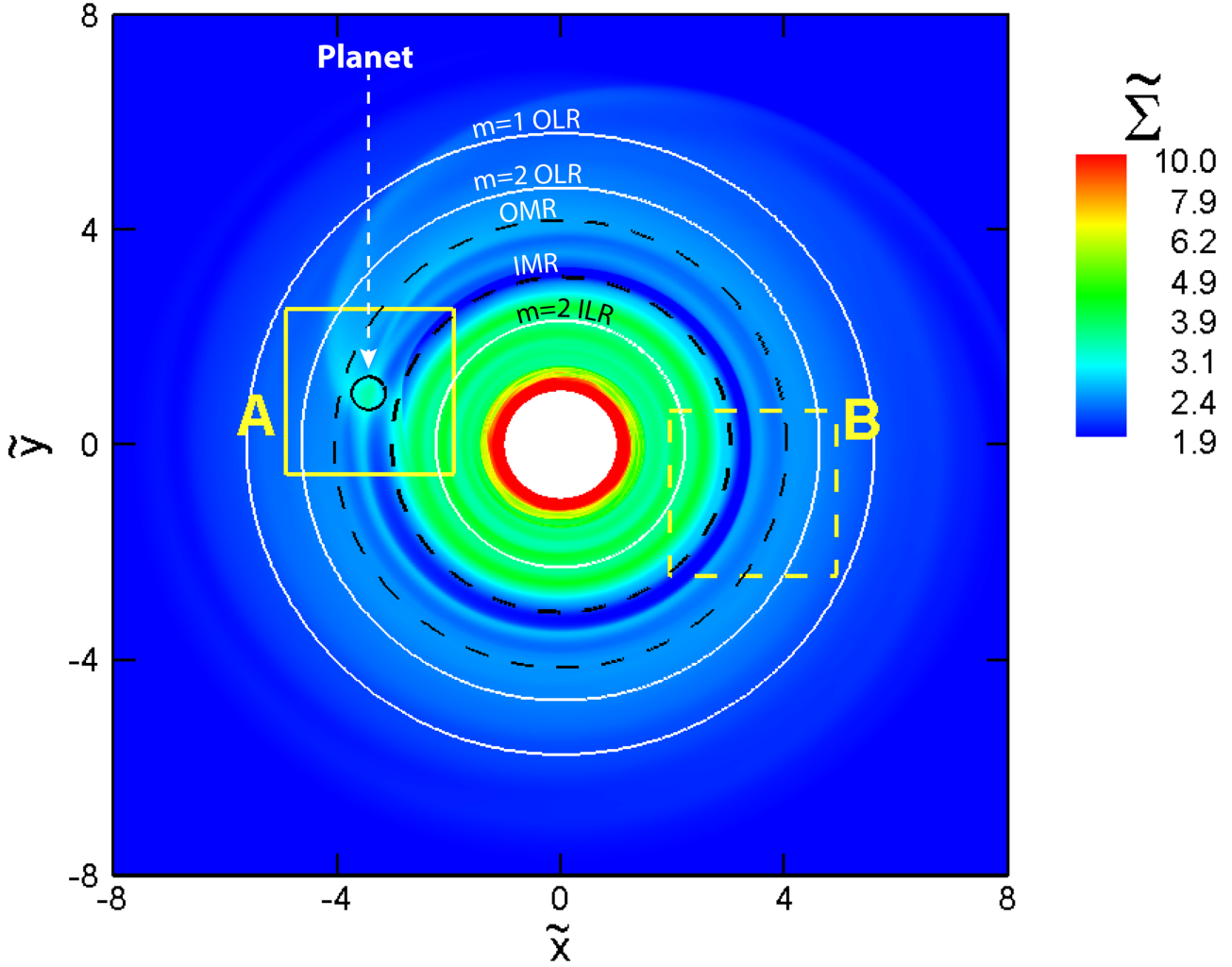


Figure 5. The surface density distribution at $\tilde{t} = 600$ for $\tilde{\mathfrak{B}}_\phi = 6/\tilde{r}$ for the case of a Jupiter-mass planet. The Lindblad resonances are marked by solid white circles, the magnetic resonances are marked by dashed black circles, and the planet’s location is indicated by a solid black circle of arbitrary size. The two highlighted regions, A and B, are examined further in Figs. 6 and 7.

distribution in the disc, the “dips” in surface density are visible.

These relatively low-density areas are more easily seen in region B (Fig. 7), without the planet nearby. In region B, the relatively high density area corresponds to a ring of material located approximately at the planet’s orbital semimajor axis that is seen on a larger scale in Fig. 5. So, there appears to be a “ring” of material near the planet’s orbital radius, with “dips” in $\tilde{\Sigma}$ on either side of the planet’s orbital radius between the magnetic resonances.

In Figs. 6 and 7, β is also relatively high near the planet’s orbital radius, and it is relatively lower elsewhere between the magnetic resonances. The “dips” in β correspond to a relatively higher magnetic pressure than matter pressure in these regions. This correspondence of lower β in regions of lower $\tilde{\Sigma}$ indicates that there is an underdensity in regions with relatively high magnetic pressure, as expected.

Figure 8 shows similar $\tilde{\Sigma}$ and β contours and one-dimensional profiles sampled along the scanlines for a Saturn-mass planet, while Figure 9 shows the same information for a

$5M_\oplus$ planet. Only the region nearby the planet is shown for the Saturn-mass and $5M_\oplus$ cases, as the perturbation to the disc from these smaller masses is small enough that the perturbations due to the MHD waves are much harder to resolve far away from the planet. The overdensity near the planet, with underdensities on the opposite sides of the planet, within the magnetic resonances is visible for both the Saturn-mass and $5M_\oplus$ planets, as it is for the Jupiter-mass planet. The magnitudes of the variations in $\tilde{\Sigma}$ and β are less visible for the Saturn-mass planet than the Jupiter-mass planet, and the variations are even smaller for the $5M_\oplus$ planet.

Overall, the magnetic resonances appear to alter the disc such that there is an underdensity (and relatively low value of β) within the magnetic resonances, while there is an overdensity (and relatively high value of β) near the planet’s orbital radius.

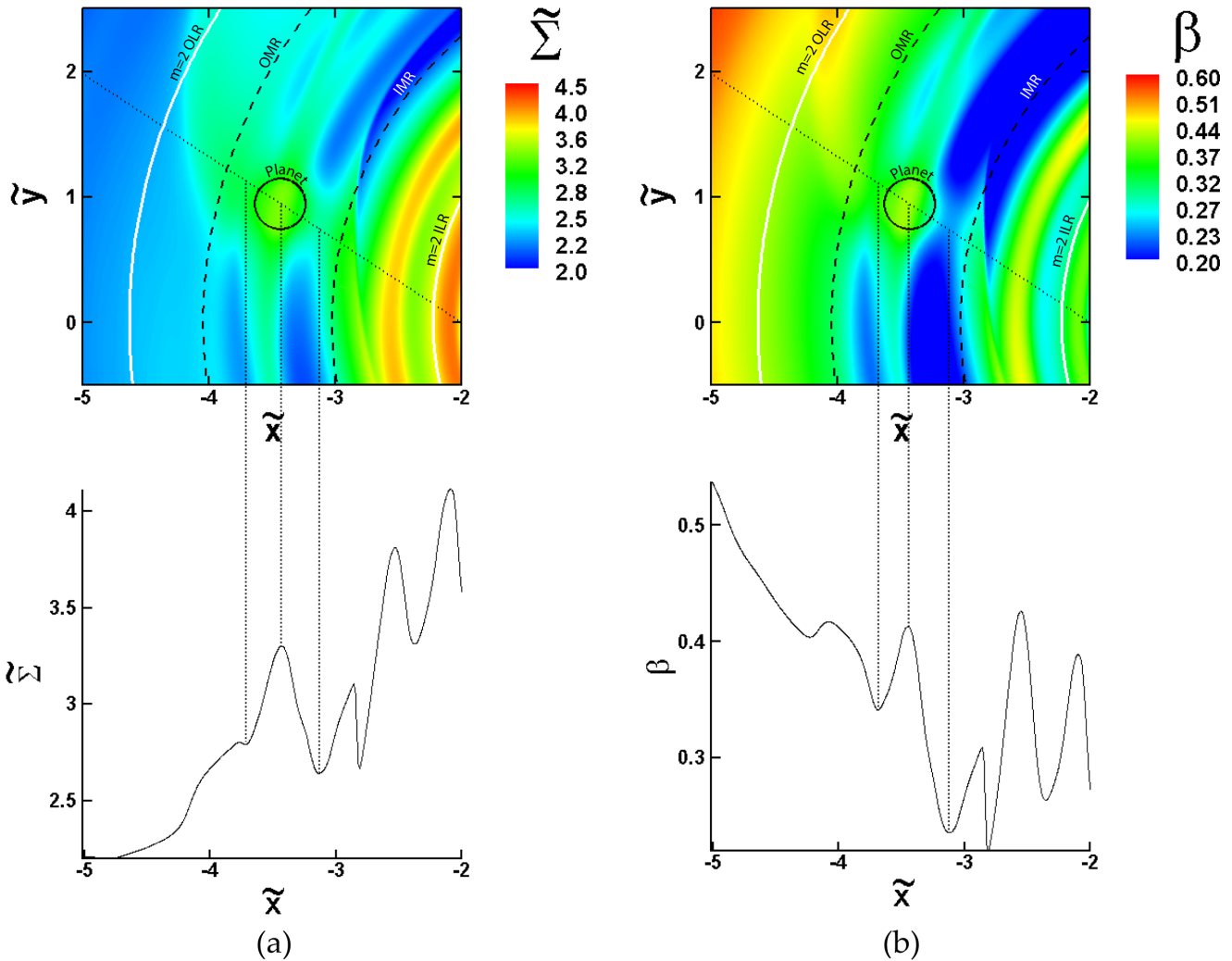


Figure 6. The (a) $\tilde{\Sigma}$ and (b) β distribution at $\tilde{t} = 600$ for $\tilde{\mathfrak{B}}_\varphi = 6/\tilde{r}$ for a Jupiter-mass planet in region A indicated in Fig. 5. The IMR, OMR, $m = 2$ OLR, and $m = 2$ ILR are labeled, as well as the location of the planet, in the top panel. $\tilde{\Sigma}$ is sampled along a scanline indicated by a straight dotted line in the top panel and plotted as a one-dimensional profile in the bottom panel of both (a) and (b). Vertical lines connecting the top and bottom panels highlight variations in $\tilde{\Sigma}$ and β between the magnetic resonances and near the planet’s orbital radius.

4 TORQUE ON THE JUPITER-MASS PLANET

Fig. 10 shows the smoothed² torque on a Jupiter-mass planet as a function of time, for several different magnetic field amplitudes. If a region is shaded red, the torque on the planet is negative and the migration is directed inward; if a region is shaded green, the torque is positive and the migration is directed outward; if a region is shaded gray, the torque is roughly zero and the migration is “stalled” (likely because the torque has saturated); and the hatched region in the hydrodynamic case indicates that the planet is no longer in the simulation region beyond that time. This figure shows that a larger magnetic field amplitude corresponds to a larger total positive torque on a Jupiter-mass planet that happens earlier,

² We smoothed the torques using iterative relaxation (Anderson et al. 1984; Isaacson & Keller 1966).

faster, and over a shorter period of time. This also implies that the torque is saturated earlier for a larger magnetic field amplitude for a Jupiter-mass planet.

So, for relatively low up to relatively high magnetic field amplitude, the torque on the Jupiter-mass planet is increasingly positive, and this torque saturates at an increasingly large orbital radius at an earlier time. This positive torque followed by saturation effectively stifles the inward differential Lindblad torque earlier for larger magnetic field amplitudes.

5 CHANGE IN THE PLANET’S ORBITAL SEMIMAJOR AXIS

Figure 11 shows the normalized change in the planet’s orbital semimajor axis over time for a Jupiter-mass, Saturn-mass, and

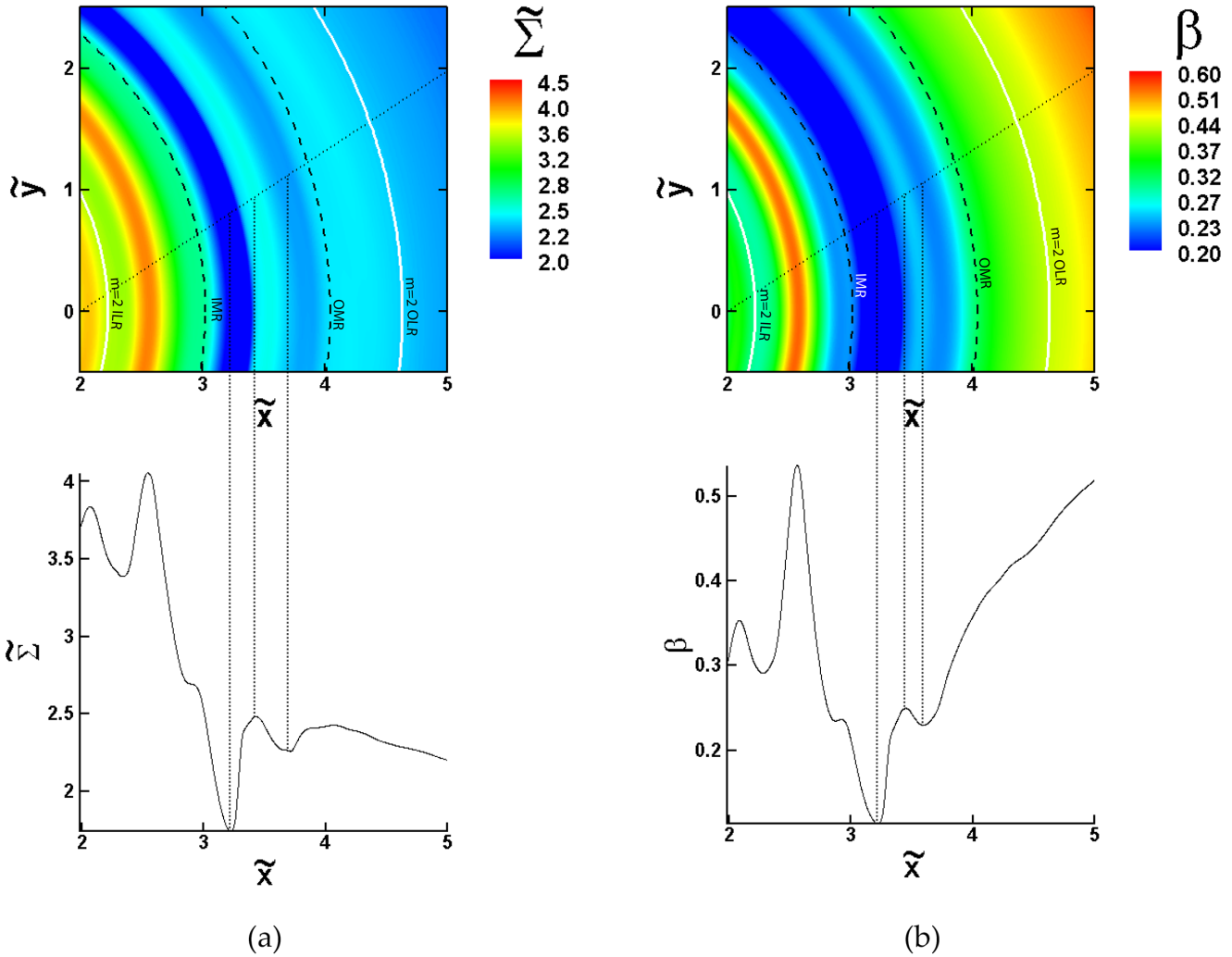


Figure 7. The (a) $\tilde{\Sigma}$ and (b) β distribution at $\tilde{t} = 600$ for $\tilde{\mathfrak{B}}_\varphi = 6/\tilde{r}$ for a Jupiter-mass planet in region B indicated in Fig. 5. The IMR, OMR, $m = 2$ OLR, and $m = 2$ ILR are labeled, as well as the location of the planet, in the top panel. $\tilde{\Sigma}$ is sampled along a scanline indicated by a straight dotted line in the top panel and plotted as a one-dimensional profile in the bottom panel of both (a) and (b). Vertical lines connecting the top and bottom panels highlight variations in $\tilde{\Sigma}$ and β between the magnetic resonances and near the planet’s orbital radius.

$5M_\oplus$ planet, respectively. Several magnetic field amplitudes are shown.

For the Jupiter-mass planet, the hydrodynamic case ($\tilde{\mathfrak{B}}_\varphi = 0$) results in rapid inward migration, as expected; the planet’s inward movement is slowed in all of the MHD cases. For relatively low magnetic field amplitudes, the Jupiter-mass planet’s migration remains inward. For larger magnetic field amplitudes, however, β is larger near and interior to the planet, and its migration slows as a result. The migration is even slightly reversed for the largest magnetic field amplitudes tested in this work.

The initial inward migration becomes slower and takes place over a shorter period of time for larger magnetic field amplitudes. The ensuing outward migration also slows, but takes place over a slightly longer period of time, for relatively low up to relatively high for magnetic field amplitude. So, for larger magnetic field amplitudes: the Jupiter-mass planet’s inward migration is slower than in cases of lower magnetic field

amplitude, and the innermost radius reached by the planet increases.

In the case of a Saturn-mass planet, the migration is also directed inward in general, but it is slowed when the magnetic field amplitude is increased. The Saturn-mass planet’s migration also reverses for the largest field amplitude similarly to the Jupiter-mass planet. For the $5M_\oplus$ planet, the migration does not reverse, but it is slightly slowed when the magnetic field amplitude is increased. The overall change in semimajor axis of the $5M_\oplus$ planet is small relative to the change seen for the Jupiter-mass and Saturn-mass planets, but there is still a noticeable change in its migration behavior.

6 DIMENSIONAL UNITS

Using Table 1, we can convert our results to dimensional units. Not reflected in Table 1, however, is the fact that we used a much higher surface density in the disc than is con-

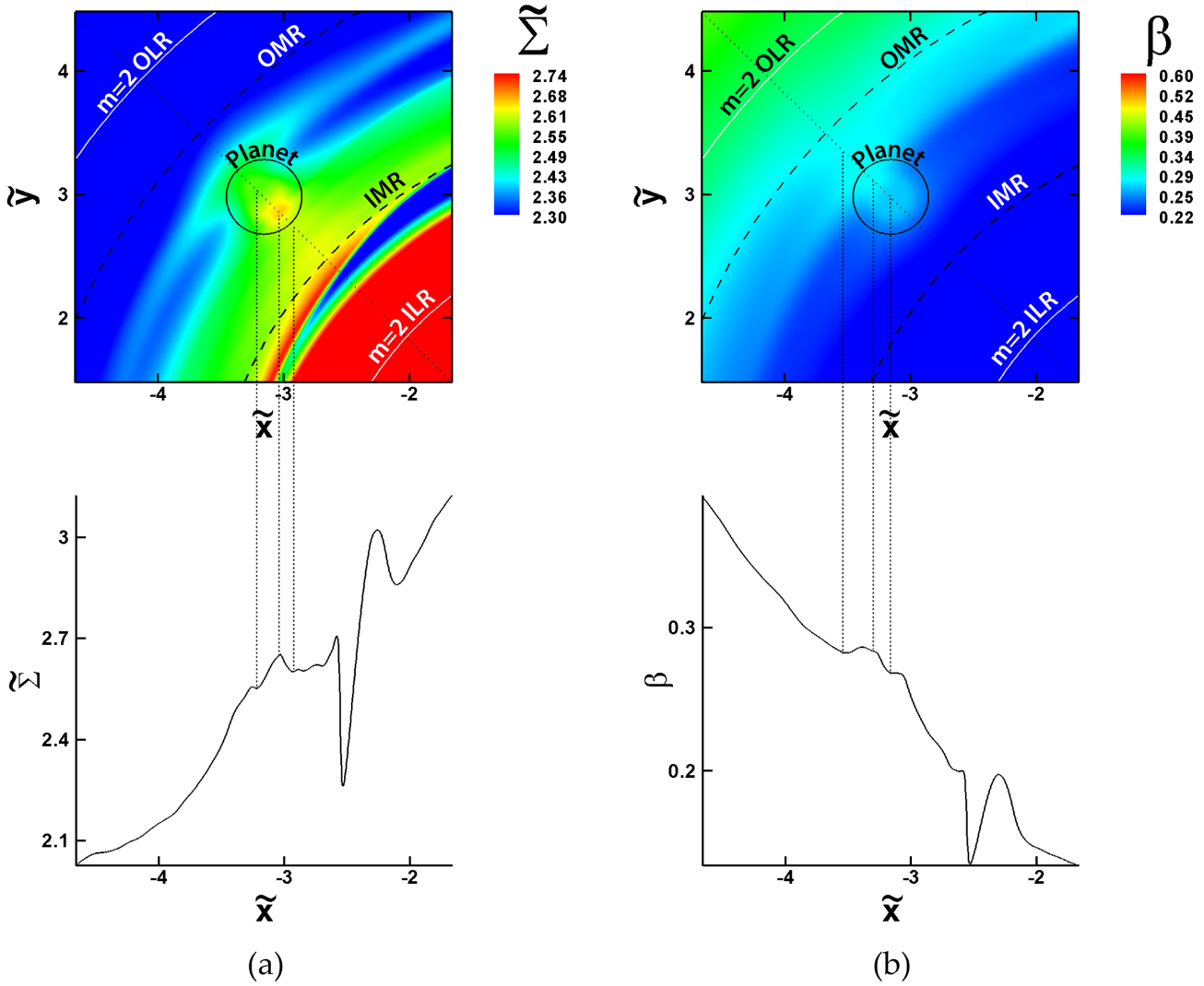


Figure 8. The (a) $\tilde{\Sigma}$ and (b) β distribution at $\tilde{t} = 420$ for $\tilde{\mathfrak{B}}_\varphi = 8/\tilde{r}$ near the planet for a Saturn-mass planet in region A indicated in Fig. 5. The IMR, OMR, $m = 2$ OLR, and $m = 2$ ILR are labeled, as well as the location of the planet, in the top panel. $\tilde{\Sigma}$ is sampled along a scanline indicated by a straight dotted line in the top panel and plotted as a one-dimensional profile in the bottom panel of both (a) and (b). Vertical lines connecting the top and bottom panels highlight variations in $\tilde{\Sigma}$ and β between the magnetic resonances and near the planet’s orbital radius.

sidered realistic. The migration time of a planet depends inversely on the surface density of the disc (Tanaka et al. 2002)³:

$$t_{\text{mig}} \propto \frac{M_\star^2}{M_p \Sigma(r_p) r_p^2 \Omega_p} \left(\frac{c}{r_p \Omega_p} \right)^2. \quad (54)$$

By using a very large surface density, our simulations require much less computational time to show appreciable planet migration. A typical protoplanetary disc surface density is $\Sigma \sim 10 \text{ g cm}^{-2}$ (e.g., Williams & Cieza 2011), while our surface density is $\Sigma \sim 10^4 \text{ g cm}^{-2}$. So, the migration times in our simulations must be multiplied by a factor of 1000 to attain a migration time relevant to realistic physical systems.

³ This is strictly true when the surface density is a power law. Our surface density is not an exact power law, but is very similar. (See Figure 1.)

Thus, in order to compare our work to realistic protoplanetary systems, we must alter our reference values for Σ_0 , B_0 , and P_0 as well: $\Sigma'_0 = \Sigma_0/1000 = 35.5 \text{ g cm}^{-2}$, $B'_0 = B_0/\sqrt{1000} = 9.2 \text{ G}$, and $P'_0 = 1000P_0 = 350 \text{ years}$. We use the value of \tilde{a} from Figure 11 to calculate the dimensional value of the planet’s semimajor axis. For example, at $t = 0$ for a Jupiter-mass planet with $\tilde{\mathfrak{B}}_\varphi = 6/\tilde{r}$, $r_p = 2.5 \text{ AU}$, $\Sigma(r_p) = 79 \text{ g cm}^{-2}$, and $B_\varphi(r_p) = 11 \text{ G}$.

That the migration time scale for a planet is larger (i.e., the average migration rate is slower) when there is a larger magnetic field amplitude in the disc is evident in Fig. 11. For example, consider the Jupiter-mass planet whose orbital radius is initially 2.5 AU. When this planet is embedded in a non-magnetic disc, its orbit decreases to 0.5 AU in approximately 8×10^4 years. However, when this planet is embedded in a disc with a magnetic field varying as $\tilde{\mathfrak{B}}_\varphi = 6/\tilde{r}$, its orbit is only reduced to 1.7 AU in the same amount of time.

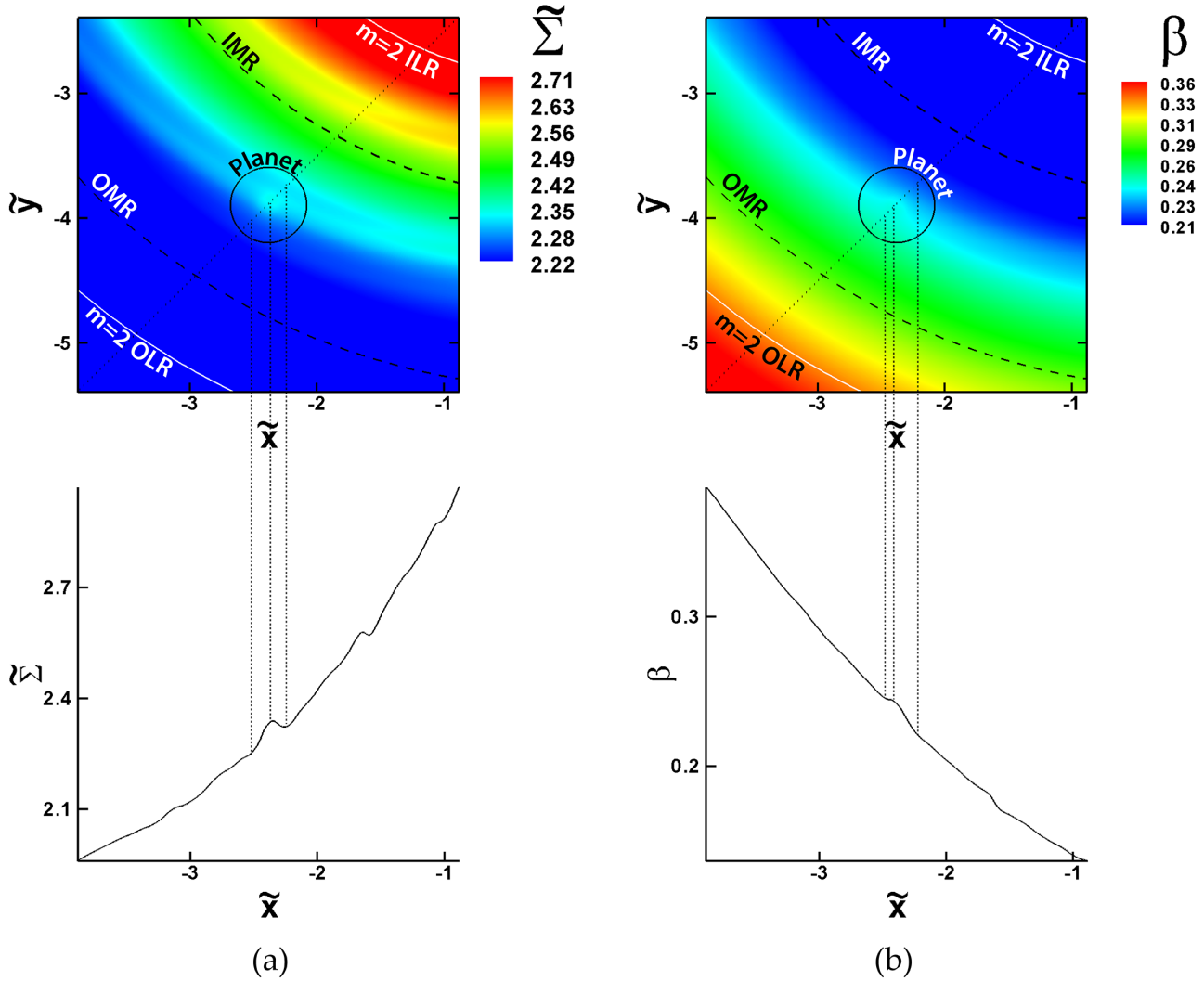


Figure 9. The (a) $\tilde{\Sigma}$ and (b) β distribution at $\tilde{t} = 300$ for $\tilde{\mathfrak{B}}_\phi = 8/\tilde{r}$ near the planet for a $5M_\oplus$ planet in region A indicated in Fig. 5. The IMR, OMR, $m = 2$ OLR, and $m = 2$ ILR are labeled, as well as the location of the planet, in the top panel. $\tilde{\Sigma}$ is sampled along a scanline indicated by a straight dotted line in the top panel and plotted as a one-dimensional profile in the bottom panel of both (a) and (b). Vertical lines connecting the top and bottom panels highlight variations in $\tilde{\Sigma}$ and β between the magnetic resonances and near the planet's orbital radius.

A more detailed description of the migration rates can be done for the case of a $5M_\oplus$ planet, because the migration direction does not change (see Table 2). From this information, it can be estimated that, for example, a $5M_\oplus$ planet will reach the surface of a $2R_\odot$ star after approximately 2.6 Myr when $\tilde{\mathfrak{B}}(\tilde{r}) = 2/\tilde{r}$, while it would reach the surface of the star after approximately 9 Myr when $\tilde{\mathfrak{B}}(\tilde{r}) = 8/\tilde{r}$.

7 DISCUSSION AND CONCLUSIONS

The main results of our paper are:

(i) In the case of not only a Jupiter-mass planet, but also Saturn-mass and $5M_\oplus$ planets, the magnetic resonances appear to alter the disc such that there is an underdensity (and relatively low value of β) within the magnetic resonances, with an overdensity (and relatively high value of β) at the planet's orbital radius. The magnitudes of the variations in Σ

$\tilde{\mathfrak{B}}(\tilde{r})$	Migration rate (AU yr ⁻¹)	Migration time to surface of star (Myr)
$2/\tilde{r}$	1.9×10^{-6}	2.6
$4/\tilde{r}$	1.5×10^{-6}	3.4
$6/\tilde{r}$	9.0×10^{-7}	5.5
$8/\tilde{r}$	5.5×10^{-7}	9.0

Table 2. Approximate average migration rates for a $5M_\oplus$ planet (corresponding to the semimajor axis changes shown in panel (c) of Figure 11), and the approximate times until the planet reaches the surface of a $2R_\odot$ star based on each of these rates.

and β are smaller in the case of a Saturn-mass planet than for the Jupiter-mass planet, and are still smaller in the case of a $5M_\oplus$ planet, but the variations are still visible relative to the background Σ and β distributions. This agrees with results presented in Terquem (2003) and Fromang et al. (2005) in

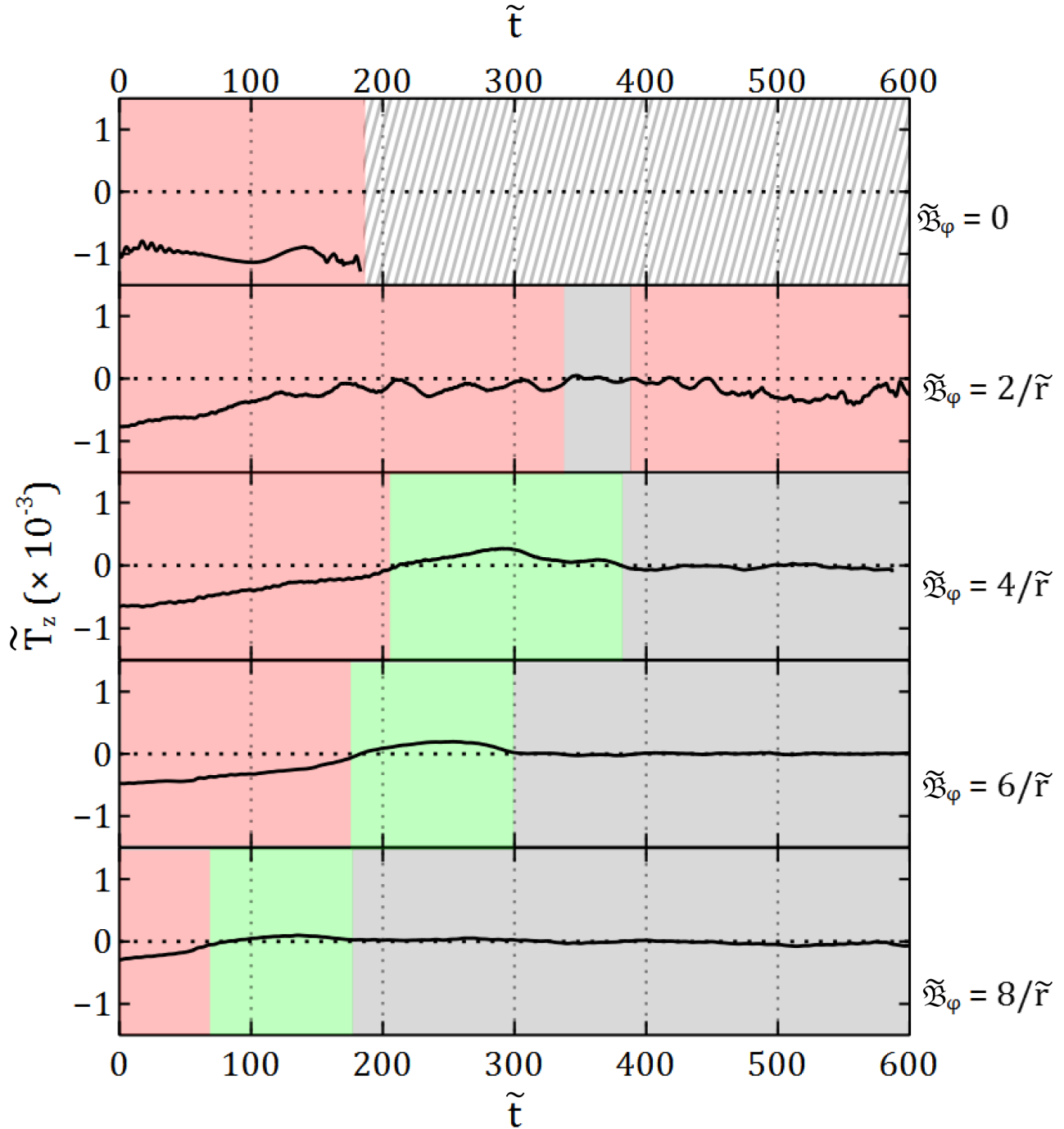


Figure 10. The change in the torque in the z direction on the Jupiter-mass planet from the disc for several magnetic field amplitudes (labeled above). The line at zero torque separates negative and positive torque; positive torque results in outward migration (shaded green) and negative torque results in inward migration (shaded red); zero torque represents a saturated torque, of which no migration is a consequence (shaded gray). The hatched region for the hydrodynamic case indicates that there is no data at those times, as the planet had already migrated beyond the inner boundary of the simulation region.

which a $5M_\oplus$ planet on a fixed circular orbit experiences a torque from the nearby magnetic resonances, and the behavior of Σ and β near the planet is similar.

(ii) For relatively low up to relatively high magnetic field amplitudes, there is an increasingly strong positive torque on the Jupiter-mass planet that happens earlier, with a cor-

responding torque saturation at earlier times, effectively reducing the effectiveness of the inwardly-directed differential Lindblad torque. The behavior of the net torque as a function of time, shown in Fig. 10 corresponds to the changes in the Jupiter-mass planet’s semimajor axis shown in Fig. 11.

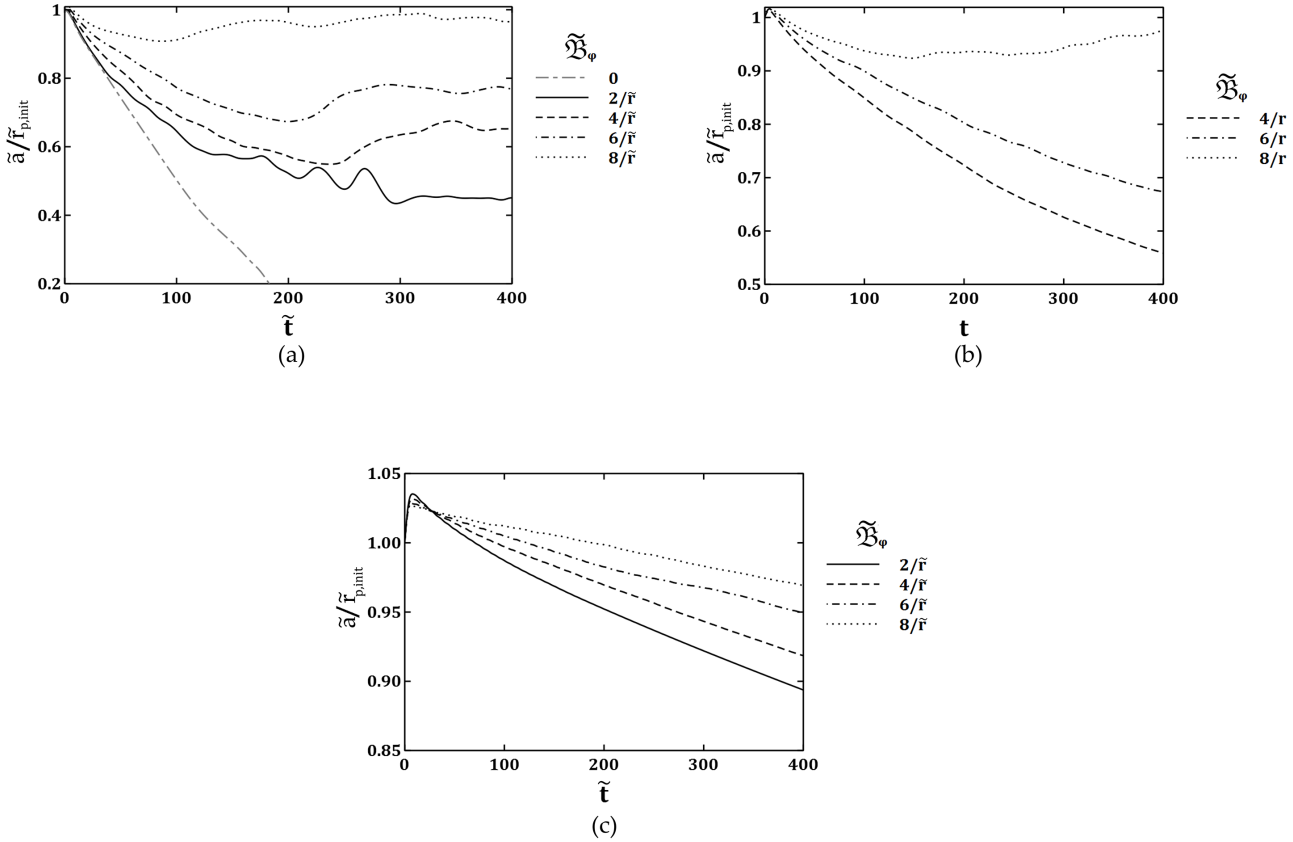


Figure 11. The normalized change in the planet's orbital semimajor axis over time. Panel (a) shows this change for a Jupiter-mass planet, panel (b) shows this change for a Saturn-mass planet, and panel (c) shows this change for a $5M_\oplus$ planet.

(iii) The planet's inward migration is slowed (and can even be reversed), and its orbit stabilizes at an increasingly large radius for a larger magnetic field amplitude. The migration both slowed and reversed for the Jupiter-mass and Saturn-mass planets, while it slowed but did not reverse for the $5M_\oplus$ planet. In our simulations, we kept the mass of the disc constant at $1M_{\text{Jup}}$, and thus the amplitudes of the excited waves are much smaller for the lower mass planets that we tested. Thus, the $5M_\oplus$ planet migrated much more slowly than the Saturn-mass and Jupiter-mass planets and never reached the region of the disc in which the magnetic field is strong enough to stop its migration.

ACKNOWLEDGEMENTS

We gratefully acknowledge support from the NASA Research Opportunities in Space and Earth Sciences (ROSES) Origins of Solar Systems grant NNX12AI85G. We also acknowledge support from grants FAP-14.B37.21.0915, SS-1434.2012.2, and RFBR 12-01-00606-a.

We also thank J. C. Mergo for valuable insight and comments.

REFERENCES

- Anderson D. A., Tannehill J. C., Pletcher R. H., 1984, Computational fluid mechanics and heat transfer. Hemisphere Publishing Corp., New York
- Baruteau C., Fromang S., Nelson R. P., Masset F., 2011, A&A, 533, A84
- Baruteau C., Masset F., 2008, ApJ, 672, 1054
- de Val-Borro M. et al., 2006, MNRAS, 370, 529
- Dyda S., Lovelace R. V. E., Ustyugova G. V., Lii P. S., Romanova M. M., Koldoba A. V., 2013, MNRAS, 432, 127
- Fromang S., Terquem C., Nelson R., 2005, MNRAS, 363, 943
- Fu W., Lai D., 2011, MNRAS, 410, 399
- Guilet J., Baruteau C., Papaloizou J. C. B., 2013, MNRAS, 430, 1764
- Isaacson E., Keller H. B., 1966, Analysis of Numerical Methods. John Wiley & Sons, New York
- Klahr H., Kley W., 2006, A&A, 445, 747
- Kley W., Bitsch B., Klahr H., 2009, A&A, 506, 971
- Masset F. S., 2001, ApJ, 558, 453
- Masset F. S., Casoli J., 2009, ApJ, 703, 857
- Masset F. S., Casoli J., 2010, ApJ, 723, 1393
- Murray C. D., Dermott S. F., 1999, Solar System Dynamics. Cambridge University Press, Cambridge
- Paardekooper S. J., Baruteau C., Crida A., Kley W., 2010, MNRAS, 401, 1950
- Paardekooper S. J., Baruteau C., Kley W., 2011, MNRAS, 410, 293

- Paardekooper S. J., Mellema G., 2006, *A&A*, 459, L17
Paardekooper S. J., Papaloizou J. C. B., 2008, *A&A*, 485, 877
Romanova M. M., Ustyugova G. V., Koldoba A. V., Lovelace
R. V. E., 2002, *ApJ*, 578, 420
Shakura N. I., Sunyaev R. A., 1973, *A&A*, 24, 337
Tanaka H., Takeuchi T., Ward W. R., 2002, *ApJ*, 565, 1257
Terquem C., 2003, *MNRAS*, 341, 1157
Uribe A. L., Klahr H., Flock M., Henning T., 2011, *ApJ*, 736,
85
Ustyugova G. V., Koldoba A. V., Romanova M. M., Lovelace
R. V. E., 2006, *ApJ*, 646, 304
Ward W. R., 1997, *Icarus*, 126, 261
Williams J. P., Cieza L. A., 2011, *A&A*, 49, 67